Available online at www.sciencedirect.com
SCIENCE DIRECT®
Journal of Computational Physics 190 (2003) 550–571
JOURNAL OF COMPUTATIONAL PHYSICS
www.elsevier.com/locate/jcp

A pressure-based algorithm for multi-phase flow at all speeds

F. Moukalled [a,*], M. Darwish [a], B. Sekar [b]

[a] *Mechanical Engineering Department, Faculty of Engineering and Architecture, American University of Beirut, P.O. Box 11-0236, Riad El Solh, Beirut 1107 2020, Lebanon*
[b] *Air Force Research Laboratory, AFRL/PRTC, Wright–Patterson AFB, OH 45433-7251, USA*

Received 28 February 2002; received in revised form 21 May 2003; accepted 26 May 2003

Abstract

A new finite volume-based numerical algorithm for predicting incompressible and compressible multi-phase flow phenomena is presented. The technique is equally applicable in the subsonic, transonic, and supersonic regimes. The method is formulated on a non-orthogonal coordinate system in collocated primitive variables. Pressure is selected as a dependent variable in preference to density because changes in pressure are significant at all speeds as opposed to variations in density, which become very small at low Mach numbers. The pressure equation is derived from overall mass conservation. The performance of the new method is assessed by solving the following two-dimensional two-phase flow problems: (i) incompressible turbulent bubbly flow in a pipe, (ii) incompressible turbulent air–particle flow in a pipe, (iii) compressible dilute gas–solid flow over a flat plate, and (iv) compressible dusty flow in a converging diverging nozzle. Predictions are shown to be in excellent agreement with published numerical and/or experimental data.

Keywords: Multi-phase flow; Pressure-based algorithm; All speed flows; Finite volume method

1. Introduction

The last two decades have witnessed a substantial transformation in the computational fluid dynamics (CFD) industry; from a research means confined to research laboratories, CFD has emerged as an every day engineering tool for a wide range of industries (Aeronautics, Automobile, chemical Processing, etc.). This increasing dependence on CFD is due to a multitude of factors that have rendered practical the simulation of large complex industrial-type problems. Some of these factors are directly related to the maturity of several numerical aspects at the *core* of CFD. These include: multi-grid acceleration techniques [1–4] with enhanced equation solvers [5,6] that have decreased the computational cost of tackling large problems, better discretization techniques with bounded high resolution schemes [13–18] yielding more accurate results, unstructured grid methods [7–12] that simplify the description of complex geometry, as

* Corresponding author. Tel.: +961-3-831-432; fax: +961-1-744-462.
E-mail addresses: memouk@aub.edu.lb (F. Moukalled), darwish@aub.edu.lb (M. Darwish), balu.sekar@wpafb.af.mil (B. Sekar).

0021-9991/$ - see front matter
doi:10.1016/S0021-9991(03)00297-3

Nomenclature

$A_{\mathrm{P}}^{(k)}, \ldots$	coefficients in the discretized equation for $\phi^{(k)}$
$B_{\mathrm{P}}^{(k)}$	source term in the discretized equation for $\phi^{(k)}$
$\mathbf{B}^{(k)}$	body force per unit volume of fluid/phase k
$C^{(k)}$	coefficient equals to $1/R^{(k)}T^{(k)}$ two-phase.
$\mathbf{D}_{\mathrm{P}}^{(k)}[\phi^{(k)}]$	matrix operator defined in Eq. (14)
$H_{\mathrm{P}}[\phi^{(k)}]$	the H operator
$\mathbf{H}_{\mathrm{P}}[\mathbf{u}^{(k)}]$	the vector form of the H_{P} operator
$\mathbf{I}^{(k)}$	inter-phase momentum transfer
$\mathbf{J}_{\mathrm{f}}^{(k)D}$	diffusion flux of $\phi^{(k)}$ across cell face 'f'
$\mathbf{J}_{\mathrm{f}}^{(k)C}$	convection flux of $\phi^{(k)}$ across cell face 'f'
$\dot{M}^{(k)}$	mass source per unit volume
P	pressure
$Pr^{(k)}, Pr_{\mathrm{t}}^{(k)}$	laminar and turbulent Prandtl number for fluid/phase k
$\dot{q}^{(k)}$	heat generated per unit volume of fluid/phase k
$Q^{(k)}$	general source term of fluid/phase k
$r^{(k)}$	volume fraction of fluid/phase k
S_{f}	surface vector
t	time
$T^{(k)}$	temperature of fluid/phase k
$U_{\mathrm{f}}^{(k)}$	interface flux velocity $(\mathbf{v}_{\mathrm{f}}^{(k)} \cdot \mathbf{S}_{\mathrm{f}})$ of fluid/phase k
$\mathbf{u}^{(k)}$	velocity vector of fluid/phase k
$u^{(k)}, v^{(k)}, \ldots$	velocity components of fluid/phase k
x, y	Cartesian coordinates
$\|\|a, b\|\|$	the maximum of a and b
Greeks	
$\rho^{(k)}$	density of fluid/phase k
$\Gamma^{(k)}$	diffusion coefficient of fluid/phase k
$\Phi^{(k)}$	dissipation term in energy equation of fluid/phase k
$\phi^{(k)}$	general scalar quantity associated with fluid/phase k
$\Delta_{\mathrm{P}}[\phi^{(k)}]$	the Δ operator
$\mu^{(k)}, \mu_{\mathrm{t}}^{(k)}$	laminar and turbulent viscosity of fluid/phase k
Ω	cell volume
δt	time step
Subscripts	
f	refers to control volume face 'f'
P	refers to the P grid point
Superscripts	
C	refers to convection contribution
D	refers to diffusion contribution
(k)	refers to fluid/phase k
$(k)*$	refers to updated value at the current iteration
$(k)0$	refers to values of fluid/phase k from the previous iteration
$(k)'$	refers to correction field of phase/fluid k
m	refers to fluid/phase m
old	refers to values from the previous time step

well as improved pressure–velocity (and density) coupling algorithms for fluid flow at all speeds [19–27] resulting in better convergence behavior. The exponential increase in microprocessors power and the associated decrease in unit cost have also benefited the CFD industry. Multiprocessor systems with large memory, set up at a fraction of the cost of the super computers of a decade ago, have pushed the limits on the size of the problems that can be tackled.

Challenges still abound in a number of fields: increasing the robustness of the employed numerical schemes, improving the accuracy of the used models, extending the many advances in the simulation of single fluid flows [28–34] to multi-phase flows [35], are just a few areas of current research interest. For multi-phase flow simulation, the basic difficulty [36] stems from the increased algorithmic complexity that need to be addressed when dealing with multiple sets of continuity and momentum equations that are inter-coupled (interchange momentum by inter-phase mass and momentum transfer, etc.) both spatially and across fluids. That is, on top of the velocity–pressure coupling for each phasic continuity–momentum set, there exist a number of inter-fluid coupling relations. This is further complicated in the simulation of supersonic multi-phase flows, or in general when developing an all speed flow multi-phase algorithm. Despite these complexities, successful segregated incompressible pressure-based solution algorithms have been devised, such as the IPSA variants developed by the Spalding Group at Imperial College [37–39] and the set of algorithms developed by the Los Alamos Scientific Laboratory (LASL) group [40–42]. For compressible flow simulations at high Mach number, special treatment is needed to resolve the density–velocity and density–pressure couplings. Algorithms for all-speed multi-phase flow simulation were recently presented and new ones derived in [36] following a Pressure-based approach but none was implemented or tested. Actually to the authors' knowledge, no work dealing with a pressure-based method capable of predicting multi-phase flow phenomena at all speeds has been reported in the literature. It is the objective of this work to test a newly developed multi-phase pressure-based solution procedure that is equally valid at all Reynolds and Mach number values.

In what follows the governing equations for compressible multi-phase flows are first presented and their discretization outlined so as to lay the ground for the derivation of the pressure correction equation, which is obtained from overall mass conservation. This class of algorithms is denoted as the mass conservation based algorithms (MCBA) [36]. Then, a brief description of the solution procedure is given and the capability of the newly developed algorithm to predict multi-phase flow at all speeds demonstrated by presenting solutions to four test problems spanning the entire subsonic to supersonic spectrum over a wide range of physical conditions (from turbulent incompressible bubbly flows to supersonic air–particle flows). The problems solved are: (i) turbulent incompressible bubbly flow in a pipe, (ii) turbulent incompressible air–particle flow in a pipe, (iii) compressible dilute air–particle flow over a flat plate, and (iv) inviscid transonic dusty flow in a converging-diverging nozzle. Furthermore, the accuracy of the method is demonstrated by comparing results against published experimental and/or numerical data.

2. The governing equations

In multi-phase flow the various fluids/phases coexist with different concentrations at different locations in the flow domain and move with unequal velocities. Thus, the equations governing multi-phase flows are the conservation laws of mass, momentum, and energy for each individual fluid. For turbulent multi-phase flow situations, an additional set of equations may be needed depending on the turbulence model used. These equations should be supplemented by a set of auxiliary relations.

The various conservation equations are:

$$\frac{\partial\left(r^{(k)}\rho^{(k)}\right)}{\partial t}+\nabla\cdot\left(r^{(k)}\rho^{(k)}\mathbf{u}^{(k)}\right)=r^{(k)}\dot{M}^{(k)}, \tag{1}$$

$$\frac{\partial\left(r^{(k)}\rho^{(k)}\mathbf{u}^{(k)}\right)}{\partial t}+\nabla\cdot\left(r^{(k)}\rho^{(k)}\mathbf{u}^{(k)}\mathbf{u}^{(k)}\right)=\nabla\cdot\left[r^{(k)}\left(\mu^{(k)}+\mu_{\mathrm{t}}^{(k)}\right)\nabla\mathbf{u}^{(k)}\right]+r^{(k)}\left(-\nabla P+\mathbf{B}^{(k)}\right)+\mathbf{I}_{M}^{(k)}, \tag{2}$$

$$\begin{aligned}&\frac{\partial\left(r^{(k)}\rho^{(k)}T^{(k)}\right)}{\partial t}+\nabla\cdot\left(r^{(k)}\rho^{(k)}\mathbf{u}^{(k)}T^{(k)}\right)\\&=\nabla\cdot\left[r^{(k)}\left(\frac{\mu^{(k)}}{Pr^{(k)}}+\frac{\mu_{\mathrm{t}}^{(k)}}{Pr_{\mathrm{t}}^{(k)}}\right)\nabla T^{(k)}\right]+\frac{r^{(k)}}{c_{P}^{(k)}}\left\{\beta^{(k)}T^{(k)}\left[\frac{\partial P}{\partial t}+\nabla\cdot\left(P\mathbf{u}^{(k)}\right)-P\nabla\cdot\left(\mathbf{u}^{(k)}\right)\right]+\Phi^{(k)}+\dot{q}^{(k)}\right\}+\frac{I_{E}^{(k)}}{c_{P}^{(k)}},\end{aligned} \tag{3}$$

where the meanings of the various terms are as given in the nomenclature.

In addition to the above mass, momentum, and energy conservation equations (1)–(3), a geometric conservation equation is needed for multi-phase flow. Physically, this equation is a statement indicating that the sum of volumes occupied by the different fluids, $r^{(k)}$, within a cell is equal to the volume of the cell containing the fluids, and is given as

$$\sum_{k}r^{(k)}=1. \tag{4}$$

Because a static mesh is used, Eq. (4) does not include a transient term.

The effect of turbulence on interfacial mass, momentum, and energy transfer is difficult to model and is still an active area of research. Similar to single-fluid flow, researchers have advertised several flow-dependent models to describe turbulence. These models vary in complexity from simple algebraic [43] models to state-of-the-art Reynolds-stress [44] models. In this work, the widely used two-equation k–ε turbulence model [45] with multi-phase specific modifications is adopted. The phasic conservation equations governing the turbulence kinetic energy (k) and turbulence dissipation rate (ε) for the kth fluid are given by

$$\frac{\partial\left(r^{(k)}\rho^{(k)}k^{(k)}\right)}{\partial t}+\nabla\cdot\left(r^{(k)}\rho^{(k)}\mathbf{u}^{(k)}k^{(k)}\right)=\nabla\cdot\left(r^{(k)}\frac{\mu_{t}^{(k)}}{\sigma_{k}^{(k)}}\nabla k^{(k)}\right)+r^{(k)}\rho^{(k)}\left(G^{(k)}-\varepsilon^{(k)}\right)+I_{k}^{(k)}, \tag{5}$$

$$\frac{\partial\left(r^{(k)}\rho^{(k)}\varepsilon^{(k)}\right)}{\partial t}+\nabla\cdot\left(r^{(k)}\rho^{(k)}\mathbf{u}^{(k)}\varepsilon^{(k)}\right)=\nabla\cdot\left(r^{(k)}\frac{\mu_{t}^{(k)}}{\sigma_{\varepsilon}^{(k)}}\nabla\varepsilon^{(k)}\right)+r^{(k)}\rho^{(k)}\frac{\varepsilon^{(k)}}{k^{(k)}}\left(c_{1\varepsilon}G^{(k)}-c_{2\varepsilon}\varepsilon^{(k)}\right)+I_{\varepsilon}^{(k)}, \tag{6}$$

where $I_{k}^{(k)}$ and $I_{\varepsilon}^{(k)}$ represent the interfacial turbulence terms. The turbulent viscosity is calculated as

$$\mu_{t}^{(k)}=C_{\mu}\rho^{(k)}\frac{\left[k^{(k)}\right]^{2}}{\varepsilon^{(k)}}. \tag{7}$$

For two-phase flows, several extensions of the k–ε model that are based on calculating the turbulent viscosity by solving the k and ε equations for the carrier or continuous phase only have been proposed in the literature [46–51]. In a recent paper, Cokljat and Ivanov [45] presented a phase coupled k–ε turbulence model, intended for the cases where a non-dilute secondary phase is present, in which the k–ε transport equations for all phases are solved. Since the method is still not well developed, the first approach in which only the k and ε equations for the carrier phase are solved is adopted in this work.

If a typical representative variable associated with phase (k) is denoted by $\phi^{(k)}$, the above conservation equations can be presented via the following general phasic equation:

$$\frac{\partial\left(r^{(k)}\rho^{(k)}\phi^{(k)}\right)}{\partial t}+\nabla\cdot\left(r^{(k)}\rho^{(k)}\mathbf{u}^{(k)}\phi^{(k)}\right)=\nabla\cdot\left(r^{(k)}\Gamma^{(k)}\nabla\phi^{(k)}\right)+r^{(k)}Q^{(k)}, \tag{8}$$

where the expression for $\Gamma^{(k)}$ and $Q^{(k)}$ can be deduced from the parent equations.

The presented set of differential equations has to be solved in conjunction with constraints on certain variables represented by algebraic relations. These auxiliary relations include the equations of state and the interfacial mass, momentum, energy, and turbulence energy transfers.

For a compressible multi-phase flow, auxiliary equations of state relating density to pressure and temperature are needed. For the kth phase, such an equation can be written as

$$\rho^{(k)} = \rho^{(k)}\left(P, T^{(k)}\right). \tag{9}$$

Several models have been developed for computing the interfacial mass, momentum, energy, and turbulence energy transfers terms. Details regarding the closures used here are given in the results section.

In order to present a complete mathematical problem, thermodynamic relations may be needed and initial and boundary conditions should supplement the above equations.

3. Discretization procedure

Integrating the general conservation Eq. (8) over a finite volume (Fig. 1) yields

$$\int_\Omega \int \frac{\partial\left(r^{(k)}\rho^{(k)}\phi^{(k)}\right)}{\partial t}\mathrm{d}\Omega + \int_\Omega \int \nabla\cdot\left(r^{(k)}\rho^{(k)}\mathbf{u}^{(k)}\phi^{(k)}\right)\mathrm{d}\Omega = \int_\Omega \int \nabla\cdot\left(r^{(k)}\Gamma^{(k)}\nabla\phi^{(k)}\right)\mathrm{d}\Omega + \int_\Omega \int r^{(k)}Q^{(k)}\,\mathrm{d}\Omega, \tag{10}$$

where Ω is the volume of the control cell (Fig. 1). Using the divergence theorem to transform the volume integral into a surface integral and then replacing the surface integral by a summation of the fluxes over the sides of the control volume, Eq. (10) is transformed to

$$\frac{\partial\left(r^{(k)}\rho^{(k)}\phi^{(k)}\Omega\right)}{\partial t} + \sum_{\mathrm{NB}=e,w,n,s,t,b}\left(\mathbf{J}_{\mathrm{NB}}^{(k)D} + \mathbf{J}_{\mathrm{NB}}^{(k)C}\right) = r^{(k)}Q^{(k)}\Omega, \tag{11}$$

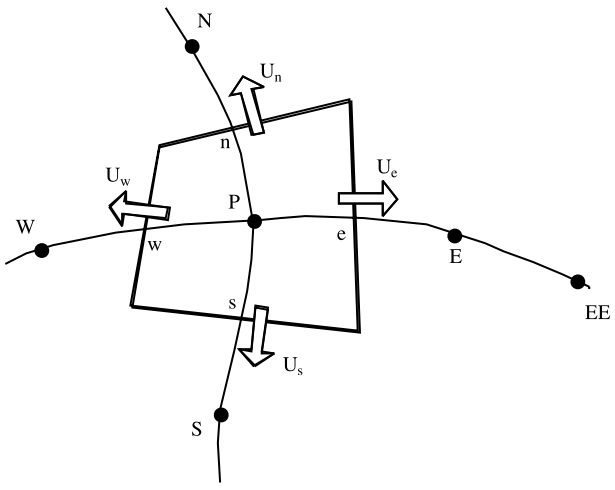

Fig. 1. Control volume.

where $\mathbf{J}_{\mathrm{NB}}^{(k)\mathrm{D}}$ and $\mathbf{J}_{\mathrm{NB}}^{(k)\mathrm{C}}$ are the diffusive and convective fluxes, respectively. The discretization of the diffusion term is second-order accurate and follows the derivations presented in [35]. For the convective terms and for the calculation of interface densities, the third-order SMART [13] scheme is employed and implemented within the context of the normalized variables and space formulation (NVSF) methodology [15]. Moreover, the integral value of the source term over the control volume is obtained by assuming the estimate of the source at the control volume center to represent the mean value over the whole control volume. Furthermore, the additional terms appearing in the momentum and energy equations, not featured in Eq. (10), are treated explicitly and their discretization is analogous to that of the ordinary diffusion flux.

Substituting the face values by the functional relationships relating them to the neighboring node values, Eq. (11) is transformed after some algebraic manipulations into the following discretized equation:

$$A_{\mathrm{P}}^{(k)}\phi_{\mathrm{p}}^{(k)} = \sum_{\mathrm{NB}} A_{\mathrm{NB}}^{(k)}\phi_{\mathrm{NB}}^{(k)} + B_{\mathrm{P}}^{(k)}, \tag{12}$$

where the coefficients $A_{\mathrm{P}}^{(k)}$ and $A_{\mathrm{NB}}^{(k)}$ depend on the selected scheme and $B_{\mathrm{P}}^{(k)}$ is the source term of the discretized equation. In compact form, the above equation can be written as

$$\phi_{\mathrm{p}}^{(k)} = H_{\mathrm{P}}\left[\phi^{(k)}\right] = \frac{\sum_{\mathrm{NB}} A_{\mathrm{NB}}^{(k)}\phi_{\mathrm{NB}}^{(k)} + B_{\mathrm{P}}^{(k)}}{A_{\mathrm{P}}^{(k)}}. \tag{13}$$

The discretization procedure for the momentum equation yields an algebraic equation of the form

$$\mathbf{u}_{\mathrm{P}}^{(k)} = \mathbf{H}_{\mathrm{P}}\left[\mathbf{u}^{(k)}\right] - r^{(k)}\mathbf{D}_{\mathrm{P}}^{(k)}\nabla_{\mathrm{P}}(P), \quad \text{where} \quad \mathbf{D}_{\mathrm{P}}^{(k)} = \begin{bmatrix} \frac{\Omega}{A_{\mathrm{P}}^{u(k)}} & 0 \\ 0 & \frac{\Omega}{A_{\mathrm{P}}^{v(k)}} \end{bmatrix}. \tag{14}$$

On the other hand, the phasic mass-conservation equation (Eq. (1)) can be either viewed as a phasic volume fraction equation

$$r_{\mathrm{p}}^{(k)} = H_{\mathrm{P}}\left[r^{(k)}\right]. \tag{15}$$

or as a phasic continuity equation to be used in deriving the pressure correction equation

$$\frac{\left(r_{\mathrm{p}}^{(k)}\rho_{\mathrm{p}}^{(k)}\right) - \left(r_{\mathrm{p}}^{(k)}\rho_{\mathrm{p}}^{(k)}\right)^{\mathrm{old}}}{\delta t}\Omega + \Delta_{\mathrm{P}}\left[r^{(k)}\rho^{(k)}\mathbf{u}^{(k)}\cdot\mathbf{S}\right] = r^{(k)}\dot{M}^{(k)}, \tag{16}$$

where the Δ operator represents the following operation:

$$\Delta_{\mathrm{P}}[\Theta] = \sum_{f=\mathrm{NB}(P)} \Theta_{\mathrm{f}}. \tag{17}$$

4. Solution procedure

The number of equations describing an n-fluid flow situation are: n-phasic momentum equations, n phasic volume fraction (or mass conservation) equations, a geometric conservation equation, and for the case of a compressible flow an additional n auxiliary pressure–density relations. Moreover, the variables involved are the n-phasic velocity vectors, the n-phasic volume fractions, the pressure field, and for a compressible flow an additional n unknown phasic density fields. In the current work, the n momentum equations are used to calculate the n velocity fields, $n-1$ volume fraction (mass conservation) equations are

used to calculate $n-1$ volume fraction fields, and the last volume fraction field calculated using the geometric conservation equation

$$r^{(n)} = 1 - \sum_{k \neq n} r^{(k)}. \tag{18}$$

The remaining volume fraction equation can be used to calculate the pressure field that is shared by all phases. However, instead of using this last volume fraction equation, in the class of mass conservation based algorithms (MCBA) the global conservation equation is employed, i.e., the sum of the individual mass conservation equations, to derive a pressure correction equation as outlined next.

4.1. The pressure correction equation

To derive the pressure correction equation, the mass conservation equations of the various phases are added to yield the global mass conservation equation given by

$$\sum_k \left\{ \frac{\left(r_{\mathrm{p}}^{(k)}\rho_{\mathrm{P}}^{(k)}\right) - \left(r_{\mathrm{p}}^{(k)}\rho_{\mathrm{P}}^{(k)}\right)^{\mathrm{old}}}{\delta t}\Omega + \Delta_{\mathrm{P}}\left(r^{(k)}\rho_{\mathrm{P}}^{(k)}\mathbf{u}^{(k)} \cdot \mathbf{S}\right) \right\} = \sum_k r^{(k)}\dot{M}^{(k)} = 0. \tag{19}$$

In the predictor stage a guessed or an estimated pressure field from the previous iteration, denoted by P^{o}, is substituted into the momentum equations. The resulting velocity fields denoted by $\mathbf{u}^{(k)*}$ which now satisfy the momentum equations will not, in general, satisfy the mass conservation equations. Thus, corrections are needed in order to yield velocity and pressure fields that satisfy both equations. Denoting the corrections for pressure, velocity, and density by P', $\mathbf{u}^{(k)'}$, and $\rho^{(k)'}$ respectively, the corrected fields are written as

$$P = P^{\mathrm{o}} + P', \quad \mathbf{u}^{(k)} = \mathbf{u}^{(k)^*} + \mathbf{u}^{(k)'}, \quad \rho^{(k)} = \rho^{(k)\mathrm{o}} + \rho^{(k)'}, \tag{20}$$

where the superscript "o" refers to values from the previous iterations. Hence the equations solved in the predictor stage are

$$\mathbf{u}_{\mathrm{P}}^{(k)^*} = \mathbf{H}_{\mathrm{P}}[\mathbf{u}^{(k)^*}] - r^{(k)\mathrm{o}}\mathbf{D}_{\mathrm{P}}^{(k)}\nabla_{\mathrm{P}}P^{\mathrm{o}}. \tag{21}$$

While the final solutions satisfy

$$\mathbf{u}_{\mathrm{P}}^{(k)} = \mathbf{H}_{\mathrm{P}}[\mathbf{u}^{(k)}] - r^{(k)}\mathbf{D}_{\mathrm{P}}^{(k)}\nabla_{\mathrm{P}}P. \tag{22}$$

Subtracting the two equation sets ((22) and (21)) from each other yields the following equation involving the correction terms:

$$\mathbf{u}_{\mathrm{P}}^{(k)} = \mathbf{H}_{\mathrm{P}}[\mathbf{u}^{(k)'}] - r^{(k)\mathrm{o}}\mathbf{D}_{\mathrm{P}}^{(k)}\nabla_{\mathrm{P}}P'. \tag{23}$$

Moreover, the new density and velocity fields, $\rho^{(k)}$ and $\mathbf{u}^{(k)}$, will satisfy the overall mass conservation equation if

$$\sum_k \left\{ \frac{\left(r_{\mathrm{p}}^{(k)\mathrm{o}}\rho_{\mathrm{P}}^{(k)}\right) - \left(r_{\mathrm{p}}^{(k)}\rho_{\mathrm{P}}^{(k)}\right)^{\mathrm{old}}}{\delta t}\Omega + \Delta_{\mathrm{P}}\left[r^{(k)\mathrm{o}}\rho^{(k)}\mathbf{u}^{(k)} \cdot \mathbf{S}\right] \right\} = 0. \tag{24}$$

Expanding the $(\rho^{(k)}\mathbf{u}^{(k)})$ term, one gets

$$\left(\rho^{(k)^*} + \rho^{(k)'}\right)\left(\mathbf{u}^{(k)^*} + \mathbf{u}^{(k)'}\right) = \rho^{(k)^*}\mathbf{u}^{(k)^*} + \rho^{(k)^*}\mathbf{u}^{(k)'} + \rho^{(k)'}\mathbf{u}^{(k)^*} + \rho^{(k)'}\mathbf{u}^{(k)'}. \tag{25}$$

Substituting Eqs. (25) and (23) into Eq. (24), rearranging, and replacing density correction by pressure correction, the final form of the pressure correction equation is written as

$$\sum_k \left\{ \frac{\Omega}{\delta t} r_{\mathrm{p}}^{(k)\mathrm{o}} C_{\rho}^{(k)} P'_{\mathrm{P}} + \Delta_{\mathrm{P}} \left[r^{(k)\mathrm{o}} U^{(k)^*} C_{\rho}^{(k)} P' \right] - \Delta_{\mathrm{P}} \left[r^{(k)\mathrm{o}} \rho^{(k)^*} \left(r^{(k)^{\circ}} \mathbf{D}^{(k)} \nabla P' \right) \cdot \mathbf{S} \right] \right\}$$
$$= -\sum_k \left\{ \frac{r_{\mathrm{p}}^{(k)\mathrm{o}} \rho_{\mathrm{P}}^{(k)^*} - \left(r_{\mathrm{p}}^{(k)} \rho_{\mathrm{P}}^{(k)} \right)^{\mathrm{old}}}{\delta t} \Omega + \Delta_{\mathrm{P}} \left[r^{(k)\mathrm{o}} \rho^{(k)^*} U^{(k)^*} \right] \right\}. \tag{26}$$

The corrections are then applied to the velocity, pressure, and density fields using the following equations:

$$\mathbf{u}_{\mathrm{P}}^{(k)^*} = \mathbf{u}_{\mathrm{P}}^{(k)\mathrm{o}} - r^{(k)\mathrm{o}} \mathbf{D}_{\mathrm{P}}^{(k)} \nabla_{\mathrm{P}} P', \quad P^* = P^{\mathrm{o}} + P', \quad \rho^{(k)^*} = \rho^{(k)\mathrm{o}} + C_{\rho}^{(k)} P'. \tag{27}$$

Numerical experiments using the above approach to simulate air–water flows have shown poor conservation of the lighter fluid. This problem can be considerably alleviated by normalizing the individual continuity equations, and hence the global mass conservation equation, by means of a weighting factor such as a reference density $\rho^{(k)}$ (which is fluid dependent). This approach has been adopted in solving all problems presented in this work (see [36] for details).

4.2. The MCBA–SIMPLE algorithm

The overall solution procedure is an extension of the single-phase SIMPLE algorithm into multi-phase flows. Since the pressure correction equation is derived from overall mass conservation, it is denoted by MCBA–SIMPLE [36]. The sequence of events in the MCBA–SIMPLE is as follows:

1. Solve the phasic momentum equations for velocities.
2. Solve the pressure correction equation based on global mass conservation.
3. Correct velocities, densities, and pressure.
4. Solve the phasic mass conservation equations for volume fractions.
5. Solve the phasic scalar equations ($k, \varepsilon, T, \ldots$).
6. Return to the first step and repeat until convergence.

5. Results and discussion

The performance of the above-described solution procedure is assessed in this section by presenting solutions to four two-dimensional two-phase flow problems spanning the entire subsonic to supersonic spectrum. The first two problems deal with incompressible turbulent flows while the last two problems are concerned with compressible flows. Computed results are compared against available experimental data and/or numerical/theoretical values. In all problems, the first phase represents the continuous phase (denoted by a superscript (c)), which must be fluid, and the second phase is the disperse phase (denoted by a superscript (d)), which may be solid particles or fluid. Unless otherwise specified the third-order SMART scheme is used in all computations reported in this study.

5.1. Problem 1: Turbulent upward bubbly flow in a pipe

The problem considered involves the prediction of radial phase distribution in turbulent upward air–water flow in a pipe. Many experimental and numerical studies addressing this problem have appeared in the literature [52–60]. Most of these studies have indicated that the lateral forces that most strongly affect

the void distribution are the turbulent stresses and the lateral lift force. As such, in addition to the usual drag force, the lift force is considered as part of the interfacial force terms in the momentum equations. In the present work, the interfacial drag forces per unit volume are given by

$$\left(I_M^x\right)_{\mathrm{D}}^{(\mathrm{c})} = -\left(I_M^x\right)_{\mathrm{D}}^{(\mathrm{d})} = 0.375\frac{C_{\mathrm{D}}}{r_{\mathrm{p}}}\rho^{(\mathrm{c})}r^{(\mathrm{d})}r^{(\mathrm{c})}V_{\mathrm{slip}}\left(u^{(\mathrm{d})}-u^{(\mathrm{c})}\right), \tag{28}$$

$$\left(I_M^y\right)_{\mathrm{D}}^{(\mathrm{c})} = -\left(I_M^y\right)_{\mathrm{D}}^{(\mathrm{d})} = 0.375\frac{C_{\mathrm{D}}}{r_{\mathrm{p}}}\rho^{(\mathrm{c})}r^{(\mathrm{d})}r^{(\mathrm{c})}V_{\mathrm{slip}}\left(v^{(\mathrm{d})}-v^{(\mathrm{c})}\right), \tag{29}$$

where r_{p} is the bubble radius. The drag coefficient C_{D} varies as a function of the bubble Reynolds and Weber numbers defined as

$$Re_{\mathrm{p}} = 2\frac{r_{\mathrm{p}}}{v_l^{(\mathrm{c})}}V_{\mathrm{slip}} \quad We = 4\rho^{(\mathrm{c})}\frac{r_{\mathrm{p}}^2}{\sigma}V_{\mathrm{slip}}, \tag{30}$$

where σ, the surface tension, is given a value of 0.072 N/m for air–water systems. The following correlations, which take the shape of the bubble into consideration, are utilized [61,62]:

$$\begin{cases} C_{\mathrm{D}} = \frac{16}{Re_{\mathrm{p}}} & \text{for } Re_{\mathrm{p}} < 0.49, \\ C_{\mathrm{D}} = \frac{20}{Re_{\mathrm{p}}^{0.643}} & \text{for } 0.49 < Re_{\mathrm{p}} < 100, \\ C_{\mathrm{D}} = \frac{6.3}{Re_{\mathrm{p}}^{0.385}} & \text{for } Re_{\mathrm{p}} \gg 100, \\ C_{\mathrm{D}} = \frac{8}{3} & \text{for } Re_{\mathrm{p}} \gg 100 \text{ and } We > 8, \\ C_{\mathrm{D}} = \frac{We}{3} & \text{for } Re_{\mathrm{p}} \gg 100 \text{ and } Re_{\mathrm{p}} > 2065.1/We^{2.6}. \end{cases} \tag{31}$$

Many investigators have considered the modeling of lift forces [61–65]. Based on their work, the following expressions are employed for the calculation of the interfacial lift forces per unit volume:

$$\left(\mathbf{I}_M\right)_{\mathrm{L}}^{(\mathrm{c})} = -\left(\mathbf{I}_M\right)_{\mathrm{L}}^{(\mathrm{d})} = C_1\rho^{(\mathrm{c})}r^{(\mathrm{d})}\left(\mathbf{u}^{(\mathrm{d})}-\mathbf{u}^{(\mathrm{c})}\right)\times\left(\nabla\times\mathbf{u}^{(\mathrm{c})}\right), \tag{32}$$

where C_1 is the interfacial lift coefficient calculated from

$$C_1 = C_{1a}\left(1-2.78\left\langle 0.2, r^{(\mathrm{d})}\right\rangle\right), \tag{33}$$

where $\langle a,b\rangle$ denotes the minimum of a and b and C_{1a} is an empirical constant.

Besides the drag and lift interfacial forces, the effect of bubbles on the turbulent field is very important, as the distribution of bubbles affects the turbulence field in the liquid phase and at the same time the liquid phase's turbulence is influenced by the bubbles. In this work, turbulence is assumed to be a property of the continuous liquid phase (c) and the turbulent kinematics viscosity of the dispersed air phase (d) is assumed to be a function of that of the continuous phase. The turbulent viscosity of the continuous phase is computed by solving the following modified transport equations for the turbulent kinetic energy k and its dissipation rate ε that take into account the interaction between the phases:

$$\begin{aligned} \frac{\partial\left(r^{(\mathrm{c})}\rho^{(\mathrm{c})}k^{(\mathrm{c})}\right)}{\partial t} + \nabla\cdot\left(r^{(\mathrm{c})}\rho^{(\mathrm{c})}\mathbf{u}^{(\mathrm{c})}k^{(\mathrm{c})}\right) &= \nabla\cdot\left[r^{(\mathrm{c})}\rho^{(\mathrm{c})}\left(v_l^{(\mathrm{c})}+\frac{v_{\mathrm{t}}^{(\mathrm{c})}}{\sigma_k^{(\mathrm{c})}}\right)\nabla k^{(\mathrm{c})}\right] + r^{(\mathrm{c})}\rho^{(\mathrm{c})}\left(G^{(\mathrm{c})}-\varepsilon^{(\mathrm{c})}\right) \\ &\quad + \nabla\cdot\left[\rho^{(\mathrm{c})}\left(\frac{v_{\mathrm{t}}^{(\mathrm{c})}}{\sigma_{\mathrm{r}}}\right)k^{(\mathrm{c})}\nabla r^{(\mathrm{c})}\right] + r^{(\mathrm{c})}P_{\mathrm{b}}, \end{aligned} \tag{34}$$

$$\frac{\partial\left(r^{(c)}\rho^{(c)}\varepsilon^{(c)}\right)}{\partial t}+\nabla\cdot\left(r^{(c)}\rho^{(c)}\mathbf{u}^{(c)}\varepsilon^{(c)}\right)=\nabla\cdot\left[r^{(c)}\rho^{(c)}\left(\nu_l^{(c)}+\frac{\nu_t^{(c)}}{\sigma_\varepsilon^{(c)}}\right)\nabla\varepsilon^{(c)}\right]+r^{(c)}c_{1\varepsilon}P_b\frac{\varepsilon^{(c)}}{k^{(c)}}$$
$$+r^{(c)}\rho^{(c)}\frac{\varepsilon^{(c)}}{k^{(c)}}\left(c_{1\varepsilon}G^{(c)}-c_{2\varepsilon}\varepsilon^{(c)}\right)+\nabla\cdot\left[\rho^{(c)}\left(\frac{\nu_t^{(c)}}{\sigma_r}\right)\varepsilon^{(c)}\nabla r^{(c)}\right], \quad (35)$$

where $G^{(c)}$ is the well-known volumetric production rate of $k^{(c)}$ by shear forces, σ_r the turbulent Schmidt number for volume fractions, and P_b is the production rate of $k^{(c)}$ by drag due to the motion of the bubbles through the liquid and is given by

$$P_b=\frac{0.375C_bC_D\rho^{(c)}r^{(d)}r^{(c)}V_{slip}^2}{r_p}. \quad (36)$$

In Eq. (36) C_b is an empirical constant representing the fraction of turbulence induced by bubbles that goes into large-scale turbulence of the liquid phase. Moreover, as suggested in [60], the flux representing the interaction between the fluctuating velocity and volume fraction is modeled via a gradient diffusion approximation and added as a source term in the continuity $(\nabla\cdot(\rho^{(k)}D^{(k)}\nabla r^{(k)}))$ and momentum $(\nabla\cdot(\rho^{(k)}D^{(k)}\mathbf{u}^{(k)}\nabla r^{(k)}))$ equations with the diffusion coefficient D given by

$$D^{(k)}=\frac{\nu_t^{(k)}}{\sigma_r}. \quad (37)$$

The turbulent kinematics eddy viscosity of the dispersed and continuous phases are related through

$$\nu_t^{(d)}=\frac{\nu_t^{(c)}}{\sigma_f}, \quad (38)$$

where σ_f is the turbulent Schmidt number for the interaction between the two phases. The above described turbulence model is a modified version of the one described in [60] in which the turbulent kinematics viscosities of both phases are allowed to be different in contrast to what is done in [60]. This is accomplished through the introduction of the σ_f parameter. As such, different diffusion coefficients ($D^{(k)}$) are used for the different phases. Results are compared to experimental data from [52,63].

Two experiments were simulated using the above-described treatment and results compared to experimental data. The two experiments differ in the Reynolds number, the bubbles diameter and the inlet conditions. In the experiment of Seriwaza et al. [52] the Reynolds number based on superficial liquid velocity and pipe diameter is 8×10^4, the inlet superficial gas and liquid velocities are 0.077 and 1.36 m/s, respectively, and the inlet void fraction is 5.36×10^{-2} with no slip between the incoming phases. Moreover, the bubble diameter is taken as 3 mm [60], while the fluid properties are taken as $\rho^{(c)}=1000$ kg/m^3, $\rho^{(d)}=1.23$ kg/m^3, and $\nu_l^{(c)}=10^{-6}$ m^2/s. In the experiment of Lahey et al. [63] the Reynolds number is based on superficial liquid velocity and pipe diameter of 5×10^4, the inlet superficial gas and liquid velocities are 0.1 and 1.08 m/s, respectively. Both problems are solved using the same values for all constants in the model with $C_{1a}=0.075$, $\sigma_f=0.5$, $\sigma_r=0.7$, and $C_b=0.05$. Predicted radial profiles of the vertical liquid velocity and void fraction presented in Figs. 2(a) and (b) using a grid of size 96×32 control volumes concur very well with measurements and compare favorably with numerical profiles reported by Boisson and Malin [60] (Fig. 2(a)) and PHOENICS [65] (Fig. 2(b)). As shown, the void fraction profile indicates that gas is taken away from the pipe center. This is caused by the lift force, which drives the bubbles towards the wall.

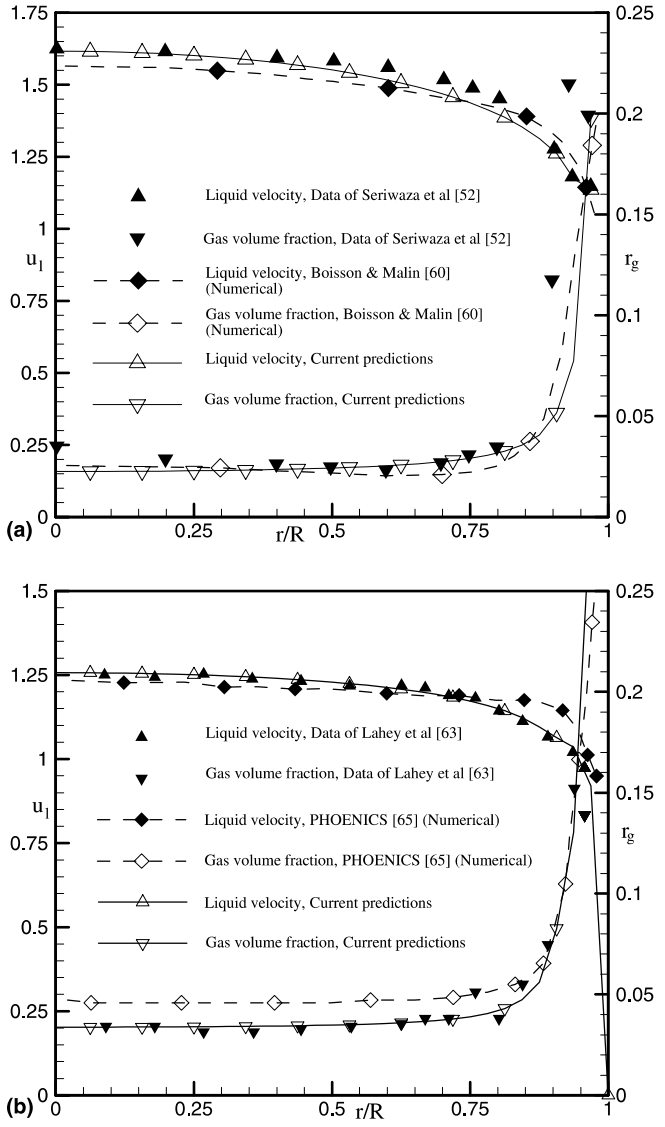

Fig. 2. Comparison of fully developed liquid velocity and void fraction profiles for turbulent bubbly upward bubbly flow in a pipe: (a) Seriwaza et al. data; (b) Lahey et al. data.

5.2. Problem 2: Turbulent air–particle flow in a vertical pipe

In problem 2, the upward flow of a dilute gas–solid mixture in a vertical pipe is simulated. As in the previous problem, the axi-symmetric form of the gas and particulate transport equations are employed. The effects of interfacial virtual mass and lift forces are small and may be neglected, as reported in several studies [66–68], and the controlling interfacial force is drag (see [69]). Denoting the continuous and dispersed phases by superscripts (c) and (d), respectively, the drag in the x- and y-momentum equations are given by

$$\left(I_M^x\right)_{\mathrm{D}}^{(\mathrm{c})} = -\left(I_M^x\right)_{\mathrm{D}}^{(\mathrm{d})} = \frac{3}{8}\frac{C_{\mathrm{D}}}{r_{\mathrm{p}}}\rho^{(\mathrm{c})}r^{(\mathrm{d})}V_{\mathrm{slip}}\left(u^{(\mathrm{d})} - u^{(\mathrm{c})}\right), \tag{39}$$

$$\left(I_M^y\right)_{\mathrm{D}}^{(\mathrm{c})} = -\left(I_M^y\right)_{\mathrm{D}}^{(\mathrm{d})} = \frac{3}{8}\frac{C_{\mathrm{D}}}{r_{\mathrm{P}}}\rho^{(\mathrm{c})}r^{(\mathrm{d})}V_{\mathrm{slip}}\left(v^{(\mathrm{d})} - v^{(\mathrm{c})}\right), \tag{40}$$

where r_{P} represents the particle's radius, C_{D} the drag coefficient computed from

$$\begin{cases} C_{\mathrm{D}} = \frac{24}{Re_{\mathrm{p}}} & \text{for } Re_{\mathrm{p}} < 1, \\ C_{\mathrm{D}} = \frac{24}{Re_{\mathrm{p}}}\left(1 + 0.15Re_{\mathrm{p}}^{0.687}\right) & \text{for } 1 < Re_{\mathrm{p}} < 1000, \\ C_{\mathrm{D}} = 0.44 & \text{for } Re_{\mathrm{p}} > 1000, \end{cases} \tag{41}$$

and Re_{p} the Reynolds number based on the particle size as defined in Eq. (30).

As before, turbulence is assumed to be a property of the continuous gas phase (c) and the turbulent kinematics viscosity of the dispersed particle phase (d) is assumed to be a function of that of the continuous phase. Again, turbulence modulation due to the presence of particles is predicted using a two-phase k–ε model. Several extensions of the k–ε model for carrier-phase turbulence modulation have been proposed in the literature [46–51] and the modification of Chen and Wood [48], which introduces additional source terms into the turbulence transport equations, is adopted here. These source terms are always negative and act to reduce k and ε. However, depending on the relative extent of reductions in k and ε, the turbulent viscosity may be either reduced or increased by the presence of particles. Thus, the turbulent viscosity is computed by solving the turbulence transport equations (Eqs. (5) and (6)) for the continuous phase with $I_k^{(\mathrm{c})}$ and $I_\varepsilon^{(\mathrm{c})}$ evaluated using the following relations suggested by Chen and Wood [48]:

$$I_k^{(\mathrm{c})} = -2\rho^{(\mathrm{d})}r^{(\mathrm{c})}r^{(\mathrm{d})}\frac{k^{(\mathrm{c})}}{\tau_{\mathrm{p}}}\left(1 - \mathrm{e}^{-0.0825(\tau_{\mathrm{p}}/\tau_{\mathrm{e}})}\right), \tag{42}$$

$$I_\varepsilon^{(\mathrm{c})} = -2\rho^{(\mathrm{d})}r^{(\mathrm{c})}r^{(\mathrm{d})}\frac{\varepsilon^{(\mathrm{c})}}{\tau_{\mathrm{p}}}, \tag{43}$$

where τ_{p} and τ_{e} are timescales characterizing the particle response and large-scale turbulent motion, respectively, and are computed from

$$\tau_{\mathrm{p}} = \frac{\rho^{(\mathrm{d})}r^{(\mathrm{d})}}{F_{\mathrm{D}}}V_{\mathrm{slip}}, \quad \tau_{\mathrm{e}} = 0.165\frac{k^{(\mathrm{c})}}{\varepsilon^{(\mathrm{c})}}, \tag{44}$$

where F_{D} is the magnitude of the inter-phase drag force per unit volume. The turbulent kinematics eddy viscosity of the dispersed phase is found using Eq. (38).

The model is validated against the experimental results of Tsuji et al. [66]. In their experiments, the vertical pipe has an internal diameter of 30.5 mm. Results are replicated here for the case of an air Reynolds number, based on the pipe diameter, of 3.3×10^4 and a mean air inlet velocity of 15.6 m/s using particles of diameter 200 μm and density 1020 kg/m^3. In the computations, the mass-loading ratio at inlet is considered to be 1 with no slip between the phases, and σ_{f} and σ_{r} are set to 5 and 10^{10} (i.e., the interaction terms included for bubbly flows are neglected here), respectively. Fig. 3 shows the fully developed gas and particles mean axial velocity profiles generated using a grid of size 96×40 CV. It is evident that there is generally a very good agreement between the predicted and experimental data with the gas velocity being slightly over predicted and the particles velocity slightly under predicted. Moreover, close to the wall, the model predictions indicate that the particles have higher velocities than the gas, which is in accord with the experimental results of Tsuji et al. [66].

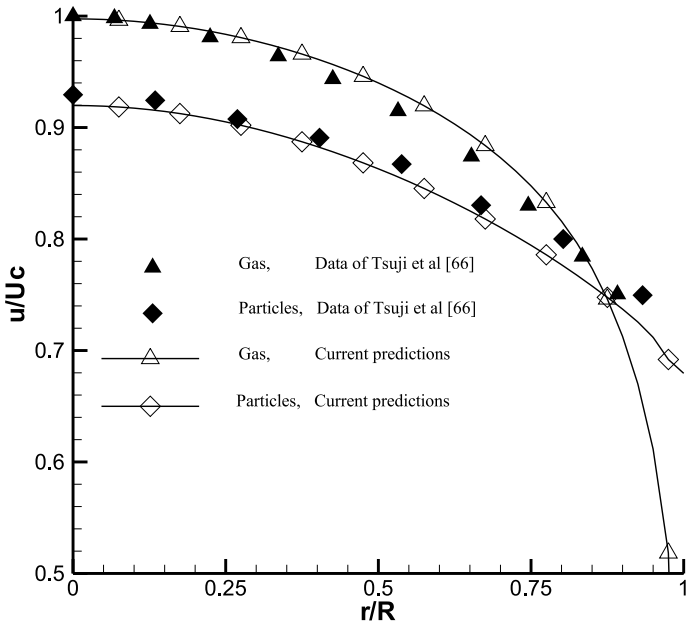

Fig. 3. Comparison of fully developed gas and particle velocity profiles for turbulent air–particle flow in a pipe.

5.3. Problem 3: Compressible dilute air–particle subsonic flow over a flat plate

This is a well-studied problem [66–76] suitable as a benchmark test. It is known that two-phase flow greatly changes the main features of the boundary layer over a flat plate. Typically, three regions are defined in the two-phase boundary layer (Fig. 4), based on the importance of the slip velocity between the two phases: a large-slip region close to the leading edge, a moderate-slip region further down, and a small-slip one far downstream. The characteristic scale in this two-phase problem is the relaxation length λ_e [73], defined as

$$\lambda_e = \frac{2}{9}\frac{\rho^{(d)} r_p^2 u_\infty}{\mu^{(c)}}, \tag{45}$$

where $\rho^{(d)}$ and r_p are, respectively, the density and radius of the particles, $\mu^{(c)}$ the viscosity of the fluid, and u_∞ the free stream velocity. The three regions are defined according to the order of magnitude of the slip parameter $x^* = x/\lambda_e$. In the simulation, the viscosity of the fluid is considered to be a function of temperature and varies according to [73]

$$\mu^{(c)} = \mu_{ref}\left(\frac{T^{(c)}}{T_{ref}}\right)^{0.6}, \tag{46}$$

where the reference viscosity and temperature are $\mu_{ref} = 1.86 \times 10^{-5}$ N s/m^2 and $T_{ref} = 303$ K, respectively. Even though variations in gas density are small under the conditions considered, these variations are not neglected and the flow is treated as compressible for the continuous phase and as incompressible for the dispersed phase. Moreover, drag is the only interfacial force retained due to its dominance over other interfacial forces. Denoting the continuous and dispersed phases by superscripts (c) and (d), respectively, this force is computed as [73]

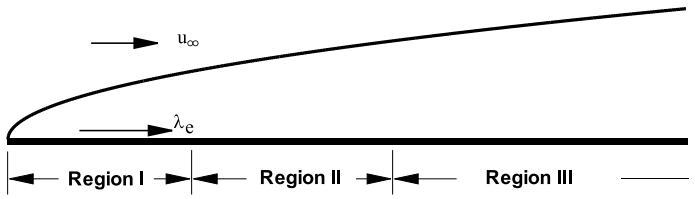

Fig. 4. The three different regions within the boundary layer of dusty flow over a flat plate.

$$\left(I_M^x\right)_{\mathrm{D}}^{(\mathrm{c})} = -\left(I_M^x\right)_{\mathrm{D}}^{(\mathrm{d})} = \frac{9}{2}\frac{C_{\mathrm{D}}}{r_{\mathrm{p}}^2} r^{(\mathrm{d})}\mu^{(\mathrm{c})}\left(u^{(\mathrm{d})} - u^{(\mathrm{c})}\right), \tag{47}$$

$$\left(I_M^y\right)_{\mathrm{D}}^{(\mathrm{c})} = -\left(I_M^y\right)_{\mathrm{D}}^{(\mathrm{d})} = \frac{9}{2}\frac{C_{\mathrm{D}}}{r_{\mathrm{p}}^2} r^{(\mathrm{d})}\mu^{(\mathrm{c})}\left(v^{(\mathrm{d})} - v^{(\mathrm{c})}\right), \tag{48}$$

where the drag coefficient is given by

$$C_{\mathrm{D}} = \frac{1}{50}Re_{\mathrm{p}} + \frac{7}{6}Re_{\mathrm{p}}^{0.15}. \tag{49}$$

In the energy equation, heat transfer due to radiation is neglected and only convective heat transfer around an isolated particle is considered. Moreover, the particles have no individual random motion, mutual collisions, and other interactions among them. Therefore, only the process of drag and heat transfer couple the particles with the gas. Under such conditions, the interfacial terms in the gas (continuous phase) and particles (dispersed phase) energy equations reduce to [73]

$$I_{\mathrm{E}}^{(\mathrm{c})} = Q_{g-p} + \mathbf{F}_{g-p}.\mathbf{u}^{(\mathrm{d})}, \tag{50}$$

$$I_{\mathrm{E}}^{(\mathrm{d})} = -Q_{g-p}, \tag{51}$$

where

$$\mathbf{F}_{\mathrm{g-p}} = \left(I_M^x\right)_{\mathrm{D}}^{(\mathrm{c})}\mathbf{i} + \left(I_M^y\right)_{\mathrm{D}}^{(\mathrm{c})}\mathbf{j}, \tag{52}$$

$$Nu = 2.0 + 0.6Re_{\mathrm{p}}^{1/2}\left(Pr^{(\mathrm{c})}\right)^{1/3}, \tag{53}$$

$$Q_{\mathrm{g-p}} = \frac{3}{2}\frac{r^{(\mathrm{d})}\lambda^{(\mathrm{c})}Nu}{r_{\mathrm{p}}^2}\left(T^{(\mathrm{d})} - T^{(\mathrm{c})}\right). \tag{54}$$

In the above equations, Nu is the Nusselt number, $Pr^{(\mathrm{c})}$ the gas Prandtl number, $\lambda^{(\mathrm{c})}$ the gas thermal conductivity, T the temperature, and other parameters are as defined earlier.

In the simulation, the particle diameter is chosen to be 10 μm, the particle Reynolds number is assumed to be equal to 10, the material density is 1766 kg/m^3, and the Prandtl number is set to 0.75. The south boundary (wall) is treated as a no-slip wall boundary for the gas phase (i.e., both components of the gas velocity are set to zero), while the particle phase encounters slip wall conditions (i.e., the normal fluxes are set to zero). The gas and the particles enter the computational domain under thermal and dynamical equilibrium conditions. A mass load ratio of 1 between the particles phase and the gas phase is used. Results are displayed using the following dimensionless variables in order to bring all quantities to the same order of magnitudes

$$x^* = \frac{x}{\lambda_e}, \quad y^* = \frac{y}{\lambda_e}\sqrt{Re}, \quad u^* = \frac{u}{u_\infty}, \quad v^* = \frac{v}{u_\infty}\sqrt{Re}, \qquad Re = \frac{\rho u \lambda_e}{\mu}. \tag{55}$$

Fig. 5 shows the results for the steady flow obtained on a rectangular domain with a mesh of density 104×48 CV. stretched in the y-direction. The figure provides the development of gas and particles velocity profiles within the three regions mentioned earlier. In the near leading edge area ($x^* = 0.1$), the gas velocity is adjusted at the wall to obtain the no-slip condition as for the case of a pure gas boundary layer. The particles have no time to adjust to the local gas motion and there is a large velocity slip between the phases. In the transition region ($x^* = 1$), significant changes in the flow properties take place. The interaction between the phases causes the particles to slow down and the gas to accelerate as apparent in the plots. In the far downstream region ($x^* = 5$), the particles have enough time to adjust to the state of the gas motion. The slip is very small and the solution tends to equilibrium. These results are in excellent agreement with the numerical solutions reported by Thevand et al. [76] plotted in Fig. 5, validating the proposed methodology.

5.4. Problem 4: Inviscid transonic dusty flow in a converging–diverging nozzle

As a final test for the newly suggested numerical procedure, dilute two-phase transonic flow in an axi-symmetric converging-diverging rocket nozzle is considered. Several researchers have analyzed the problem and data is available for comparison [77–86]. In most of the reported studies, a shorter diverging section, in comparison with the one considered here, has been used when predicting the two-phase flow. Two-phase results for the long configuration have only been reported by Chang et al. [81]. The flow is assumed to be inviscid and the single-phase results are used as an initial guess for solving the two-phase problem. The physical configuration (Fig. 6) is the one described in [81]. The viscosity of the fluid, which is solely used in the calculation of the interfacial drag force, varies with the temperature according to Sutherland's law for air

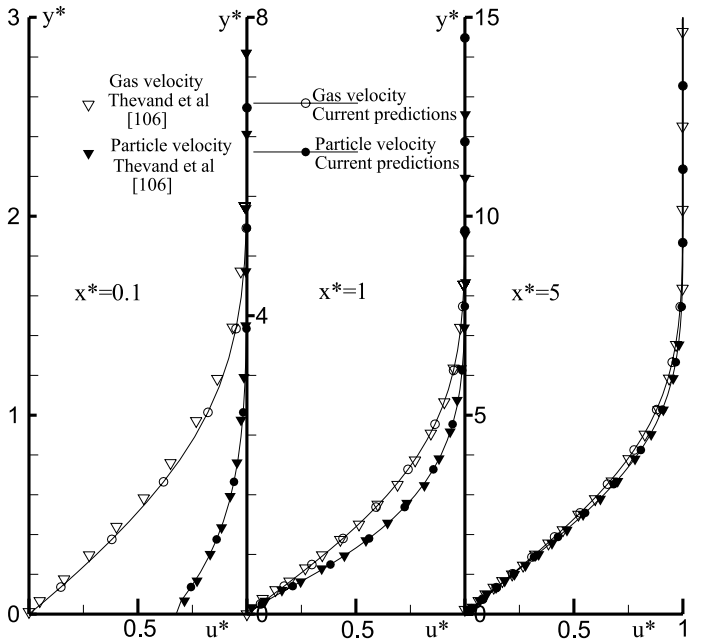

Fig. 5. Comparison of fully developed gas and particle velocity profiles inside the boundary layer at different axial locations for dilute two-phase flow over a flat plate.

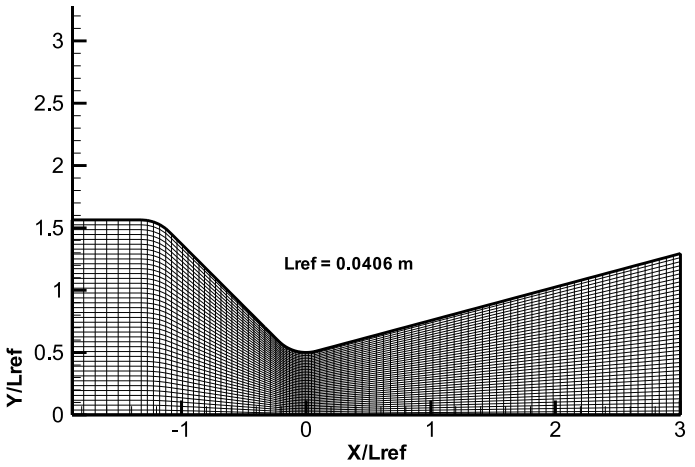

Fig. 6. Physical domain for the dusty gas flow in a converging–diverging nozzle.

$$\mu^{(c)} = 1.458 \times 10^{-6} \frac{T^{(c)}\sqrt{T^{(c)}}}{T^{(c)} + 110.4}. \tag{56}$$

The coupling between gas and particle phases is through the interfacial momentum and energy terms. The force exerted on a single particle moving through a gas is given as [82]

$$f_x = 6\pi r_p f_D \mu^{(c)} \left(u^{(d)} - u^{(c)}\right), \tag{57}$$

$$f_y = 6\pi r_p f_D \mu^{(c)} \left(v^{(d)} - v^{(c)}\right), \tag{58}$$

so that for N particles in a unit volume the effective drag force is

$$\left(I_M^x\right)_D^{(c)} = -\left(I_M^x\right)_D^{(d)} = \frac{9}{2}\frac{r^{(d)}}{r_p^2} f_D \mu^{(c)} \left(u^{(d)} - u^{(c)}\right), \tag{59}$$

$$\left(I_M^y\right)_D^{(c)} = -\left(I_M^y\right)_D^{(d)} = \frac{9}{2}\frac{r^{(d)}}{r_p^2} f_D \mu^{(c)} \left(v^{(d)} - v^{(c)}\right), \tag{60}$$

where f_D is the ratio of the drag coefficient C_D to the stokes drag $C_{D0} = 24/Re_p$ and is given by [81]

$$f_D = 1 + 0.15 Re_p^{0.687} + \frac{0.0175 Re_p}{1 + 4.25 \times 10^4 Re_p^{-1.16}}, \quad Re_p < 3 \times 10^5. \tag{61}$$

The heat transferred from gas to particle phase per unit volume is given as [82]

$$Q_{g\text{–}p} = \frac{3}{2}\frac{r^{(d)}}{r_p} \lambda^{(c)} Nu \left(T^{(d)} - T^{(c)}\right), \tag{62}$$

where $\lambda^{(c)}$ is the thermal conductivity of the gas and Nu, the Nusselt number, is written as [82]

$$Nu = 2 + 0.459 Re_p^{0.55} Pr_c^{0.33}. \tag{63}$$

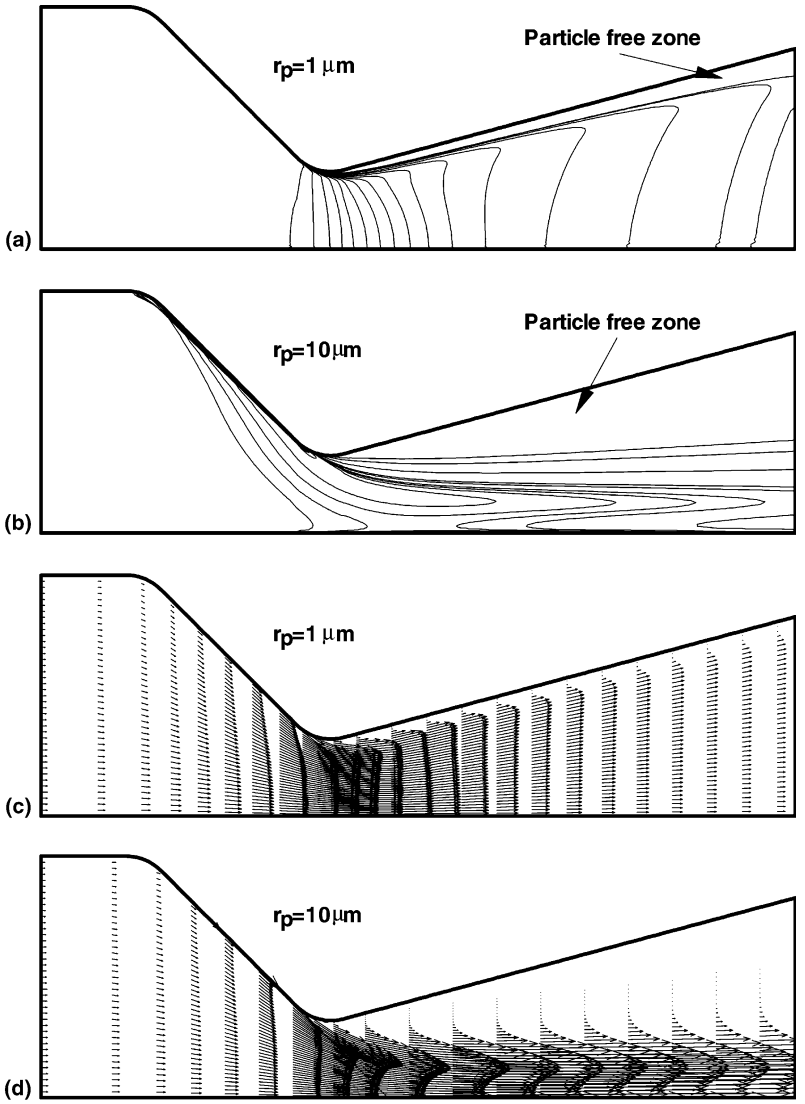

Fig. 7. (a,b) Volume fraction contours and (c,d) particle velocity vectors for dusty gas flow in a converging–diverging nozzle.

The gas–particle inter-phase energy term is given by

$$I_{\mathrm{E}}^{(\mathrm{c})} = \frac{9}{2}\frac{r^{(\mathrm{d})}}{r_{\mathrm{p}}^2} f_{\mathrm{D}} \mu^{(\mathrm{c})} \left(u^{(\mathrm{d})} - u^{(\mathrm{c})}\right) u_{\mathrm{d}} + \frac{9}{2}\frac{r^{(\mathrm{d})}}{r_{\mathrm{p}}^2} f_{\mathrm{D}} \mu^{(\mathrm{c})} \left(v^{(\mathrm{d})} - v^{(\mathrm{c})}\right) v_{\mathrm{d}} + \frac{3}{2}\frac{r^{(\mathrm{d})}}{r_{\mathrm{p}}} \lambda^{(\mathrm{c})} Nu \left(T^{(\mathrm{d})} - T^{(\mathrm{c})}\right), \tag{64}$$

$$I_{\mathrm{E}}^{(\mathrm{d})} = \frac{3}{2}\frac{r^{(\mathrm{d})}}{r_{\mathrm{p}}} \lambda^{(\mathrm{c})} Nu \left(T^{(\mathrm{c})} - T^{(\mathrm{d})}\right), \tag{65}$$

where the first two terms on the right-hand side of Eq. (64) represent the energy exchange due to momentum transfer.

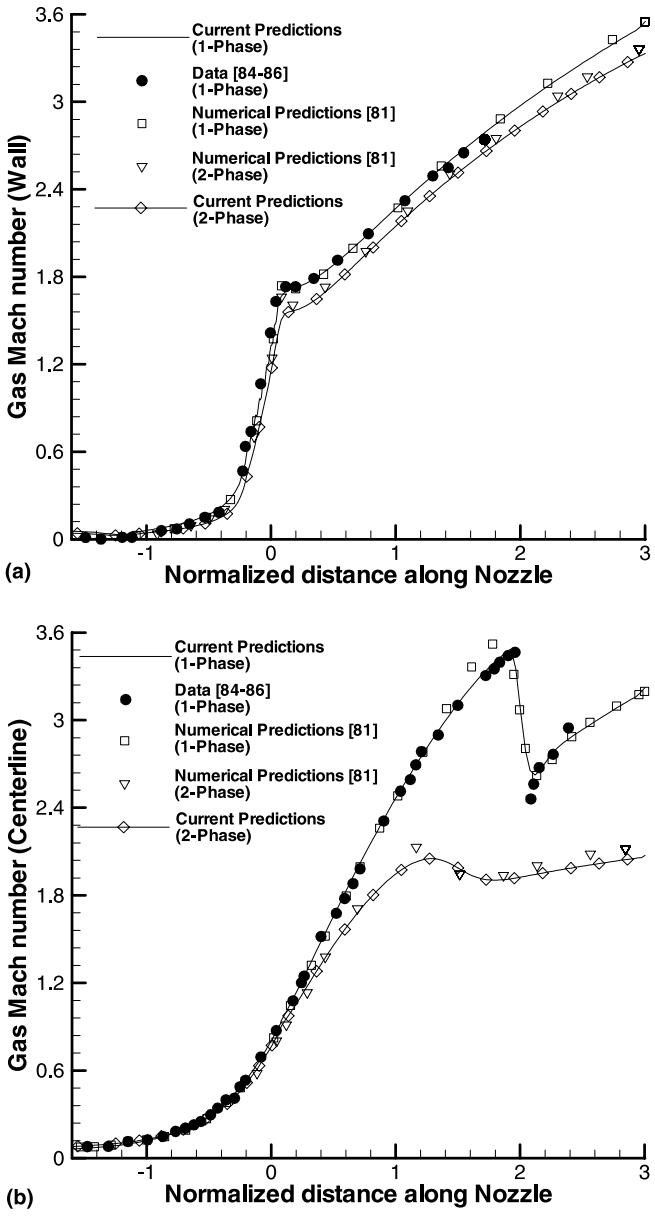

Fig. 8. Comparison of one-phase and two-phase gas Mach number distributions along the (a) wall and (b) centerline of the dusty flow in a converging–diverging nozzle problem.

The physical quantities employed are similar to those used in [81]. The gas stagnation temperature and pressure at inlet to the nozzle are 555 K and 10.34×10^5 N/m^2, respectively. The specific heat for the gas and particles are 1.07×10^3 J/kg K and 1.38×10^3 J/kg K, respectively, and the particle density is 4004.62 kg/m^3. With a zero inflow velocity angle, the fluid is accelerated from subsonic to supersonic speed in the nozzle. The inlet velocity and temperature of the particles are presumed to be the same as those of the gas phase. Results for two particle sizes of radii 1 and 10 μm with the same mass fraction $\phi = 0.3$ are presented using a

grid of size 188×80 CV. Figs. 7(a) and (b) show the particle volume fraction contours while Figs. 7(c) and (d) display the velocity distribution. For the flow with particles of radius 1 μm, a sharp change in particle density is obtained near the upper wall downstream of the throat, and the particle density decreases to a small value. With the large particle flow (10 μm), however, a much larger particle-free zone appears due to the inability of the heavier particles to turn around the throat corner. These findings are in excellent agreement with published results reported in [81] and others using different methodologies. In addition the contour lines are similar to those reported by Chang et al. [81]. A quantitative comparison of current predictions with published experimental and numerical data is presented in Fig. 8 through gas Mach number distributions along the wall (Fig. 8(a)) and centerline (Fig. 8(b)) of the nozzle for the one-phase and two-phase flow situations with particles of radii 10 μm. As can be seen, the one-phase predictions fall on top of experimental data reported in [84–86]. Along the centerline of the nozzle, current predictions are of quality better than those obtained by Chang et al. [81]. Since the nozzle contour has a rapid contraction followed by a throat with a small radius of curvature, the flow near the throat wall is overturned and inclined to the downstream wall. A weak shock is thus formed to turn the flow parallel to the wall. This results in a sudden drop in the Mach number value and as depicted in Fig. 8(b), this sudden drop is correctly envisaged by the solution algorithm with the value after the shock being slightly over predicted.

Due to the unavailability of two-phase flow data, predictions are compared against the numerical results reported in [81]. As displayed in Figs. 8(a) and (b), both solutions are in good agreement with each other indicating once more the correctness of the calculation procedures. The lower gas Mach number in the two-phase flow is caused by the heavier particles ($\rho^{(d)} \gg \rho^{(c)}$), which reduce the gas velocity. Moreover, owing to the particle-free zone, the Mach number difference between the one- and two-phase flows along the wall is smaller than that at the centerline.

6. Closing remarks

A new finite volume-based numerical procedure for the calculation of multi-phase flows at all speeds was presented. The virtues of the method were demonstrated by solving four two-phase flow problems spanning the entire subsonic to supersonic spectrum over a wide range of physical conditions: turbulent bubbly flow in a pipe, turbulent air–particle flow in a pipe, subsonic compressible air–particle flow over a flat plate, and transonic dusty flow in a converging diverging nozzle. Results generated were compared against experimental and/or numerical simulation data where available. The accuracy of the predicted quantities, which was shown to be similar or better than that obtained with special purpose methods, was a clear demonstration of the effectiveness of the new method as a tool for modeling multi-phase flows at all speeds.

Acknowledgements

The financial support provided by the European Office of Aerospace Research and Development (EOARD) (SPC00-4071) is gratefully acknowledged.

References

[1] A. Brandt, Multi-level adaptive solutions to boundary-value problems, Math. Comp. 31 (1977) 333–390.
[2] C.M. Rhie, A pressure based Navier–Stokes solver using the multigrid method, AIAA Paper 86-0207, 1986.
[3] P. Wesseling, An Introduction to Multigrid Methods, Wiley, Baffins Lane, Chichester, West Sussex PO19 1UD, UK, 1995.
[4] E. Dick, Multigrid formulation of polynomial flux-difference splitting for steady Euler equations, J. Comput. Phys. 91 (1990) 161–173.

[5] D. Kershaw, The incomplete Cholesky-conjugate gradient method for the iterative solution of systems of linear equations, J. Comput. Phys. 26 (1978) 43–65.
[6] H.L. Stone, Iterative solution of implicit approximations of multidimensional partial differential equations, SIAM J. Numer. Anal. 5 (3) (1968) 530–558.
[7] V. Venkatakrishnan, D.J. Mavriplis, Implicit method for the computation of unsteady flows on unstructured grids, AIAA Paper 95-1705, 1995.
[8] V. Venkatakrishnan, Perspective on unstructured grid solvers, AIAA J. 34 (3) (1996) 533–547.
[9] D.L. Whitaker, Three dimensional unstructured grid Euler computations using a fully-implicit, upwind method, AIAA Paper 93-3357, 1993.
[10] D. Oan, J.C. Cheng, Upwind finite volume Navier–Stokes computations on unstructured triangular meshes, AIAA J. 31 (9) (1993) 1618–1625.
[11] C.R. Mitchell, Improved reconstructuion schemes for the Navier–Stokes equations on unstructured grids, AIAA Paper 94-0642, 1994.
[12] T.J. Barth, D.C. Jespersen, The design and application of upwind schemes on unstructured meshes, AIAA Paper 89-0366, January 1989.
[13] P.H. Gaskell, A.K.C. Lau, Curvature compensated convective transport: SMART, a new boundedness preserving transport algorithm, Int. J. Numer. Methods Fluids 8 (1988) 617–641.
[14] B.P. Leonard, Locally modified quick scheme for highly convective 2-D and 3-D flows, in: C. Taylor, K. Morgan (Eds.), Numerical Methods in Laminar and Turbulent Flows, 15, Pineridge Press, Swansea, UK, 1987, pp. 35–47.
[15] M.S. Darwish, F. Moukalled, Normalized variable and space formulation methodology for high-resolution schemes, Numer. Heat Transfer, Part B 26 (1994) 79–96.
[16] F. Moukalled, M.S. Darwish, A new family of streamline-based very high resolution schemes, Numer. Heat Transfer 32 (3) (1997) 299–320.
[17] M. Darwish, F. Moukalled, An efficient very high-resolution scheme based on an adaptive-scheme strategy, Numer. Heat Transfer, Part B 34 (1998) 191–213.
[18] F. Moukalled, M. Darwish, New family of adaptive very high resolution schemes, Numer. Heat Transfer, Part B 34 (1998) 215–239.
[19] C.H. Marchi, C.R. Maliska, A non-orthogonal finite-volume methods for the solution of all speed flows using co-located variables, Numer. Heat Transfer, Part B 26 (1994) 293–311.
[20] I. Demirdzic, Z. Lilek, M. Peric, A collocated finite volume method for predicting flows at all speeds, Int. J. Numer. Methods Fluids 16 (1993) 1029–1050.
[21] F.S. Lien, M.A. Leschziner, A general non-orthogonal collocated finite volume algorithm for turbulent flow at all speeds incorporating second-moment turbulence-transport closure, Part 1: computational implementation, Comput. Methods Appl. Mech. Eng. 114 (1994) 123–148.
[22] E.S. Politis, K.C. Giannakoglou, A pressure-based algorithm for high-speed turbomachinery flows, Int. J. Numer. Methods Fluids 25 (1997) 63–80.
[23] K.H. Chen, R.H. Pletcher, Primitive variable, strongly implicit calculation procedure for viscous flows at all speeds, AIAA J. 29 (8) (1991) 1241–1249.
[24] M. Darbandi, G.E. Shneider, Momentum variable procedure for solving compressible and incompressible flows, AIAA J. 35 (12) (1997) 1801–1805.
[25] M. Darbandi, G.E. Schneider, Use of a flow analogy in solving compressible and incompressible flows, AIAA Paper 97-2359, January 1997.
[26] K.C. Karki, A calculation procedure for viscous flows at all speeds in complex geometries, Ph.D. Thesis, University of Minnesota, June 1986.
[27] F. Moukalled, M. Darwish, A high-resolution pressure-based algorithm for fluid flow at all speeds, J. Comput. Phys. 168 (1) (2001) 101–133.
[28] S.V. Patankar, D.B. Spalding, A calculation procedure for heat, mass and momentum transfer in three dimensional parabolic flows, Int. J. Heat Mass Transfer 15 (1972) 1787.
[29] S.V. Patankar, Numerical Heat Transfer and Fluid Flow, Hemisphere, Washington DC, 1981.
[30] R.I. Issa, Solution of the implicit discretized fluid flow equations by operator splitting, Mechanical Engineering Report, FS/82/15, Imperial College, London, 1982.
[31] J.P. Van Doormaal, G.D. Raithby, Enhancement of the SIMPLE method for predicting incompressible fluid flows, Numer. Heat Transfer 7 (1984) 147–163.
[32] J.P. Van Doormaal, G.D. Raithby, An evaluation of the segregated approach for predicting incompressible fluid flows, ASME Paper 85-HT-9, Presented at the National Heat Transfer Conference, Denver, CO, August 4–7, 1985.
[33] S. Acharya, F. Moukalled, Improvements to incompressible flow calculation on a non-staggered curvilinear grid, Numer. Heat Transfer, Part B 15 (1989) 131–152.

[34] C.R. Maliska, G.D. Raithby, Calculating 3-D fluid flows using non-orthogonal grid, Proc. Third Int. Conf. on Numerical Methods in Laminar and Turbulent Flows, Seattle, 1983, pp. 656–666.
[35] F. Moukalled, M. Darwish, A unified formulation of the segregated class of algorithms for fluid flow at all speeds, Numer. Heat Transfer, Part B 37 (1) (2000) 103–139.
[36] M. Darwish, F. Moukalled, B. Sekar, A unified formulation of the segregated class of algorithms for multi-fluid flow at all speeds, Numer. Heat Transfer, Part B 40 (2) (2001) 99–137.
[37] D.B. Spalding, The Calculation of free-convection phenomena in gas-liquid mixtures, Report HTS/76/11, Mech. Eng. Imperial College, London, 1976.
[38] D.B. Spalding, Numerical computation of multi-phase fluid flow and heat transfer, in: C. Taylor, K. Morgan (Eds.), Recent Advances in Numerical Methods in Fluid, 1, 1980, pp. 139–167.
[39] D.B. Spalding, A general purpose computer program for multi-dimensional, one and two phase flow, Report HTS/81/1, Mech. Eng. Imperial College, London, 1981.
[40] W.W. Rivard, M.D. Torrey, KFIX: A program for transient two dimensional two fluid flow, Report LA-NUREG-6623, 1978.
[41] A.A. Amsden, F.H. Harlow, KACHINA: An Eulerian computer program for multifield flows, Report LA-NUREG-5680, 1975.
[42] A.A. Amsden, F.H. Harlow, KTIFA two-fluid computer program for down comer flow dynamics, Report LA-NUREG-6994, 1977.
[43] B.S. Baldwin, H. Lomax, Thin Layer approximation and algebraic model for separated turbulent flows, AIAA Paper 78-257, 1978.
[44] F. Sotiropoulos, V.C. Patel, Application of Reynolds-stress transport models to stern and wake flow, J. Ship Res. 39 (1995) 263.
[45] D. Cokljat, V.A. Ivanov, F.J. Srasola, S.A. Vasquez, Multiphase k–ε models for unstructured meshes, ASME 2000 Fluids Engineering Division Summer Meeting, June 11–15, 2000, Boston, MA, USA.
[46] F. Pourahmadi, J.A.C. Humphrey, Modeling solid–fluid turbulent flows with application to predicting erosive wear, Int. J. Phys. Chem. Hydro. 4 (1983) 191–219.
[47] S.E. Elghobashi, T.W. Abou-Arab, A two-equation turbulence model for two-phase flows, Phys. Fluids 26 (4) (1983) 931–938.
[48] C.P. Chen, P.E. Wood, Turbulence closure modeling of the dilute gas–particle axisymmetric jet, AIChE J. 32 (1) (1986) 163–166.
[49] M. Lopez de Bertodano, S.J. Lee, R.T. Lahey Jr., D.A. Drew, The prediction of two-phase turbulence and phase distribution phenomena using a Reynolds stress model, ASME J. Fluids Eng. 112 (1990) 107–113.
[50] M. Lopez de Bertodano, R.T. Lahey Jr., O.C. Jones, Development of a k–ε model for bubbly two-phase flow, ASME J. Fluids Eng. 116 (1994) 128–134.
[51] M. Lopez de Bertodano, R.T. Lahey Jr., O.C. Jones, Phase distribution in bubbly two-phase flow in vertical ducts, Int. J. Multiphase flow 20 (5) (1994) 805–818.
[52] A. Serizawa, I. Kataoka, I. Michiyoshi, Phase distribution in bubbly flow, Data set No. 24, Proc. Second Int. Workshop on Two-Phase Flow Fundamentals, Rensselaer Polytechnic Institute, Troy, NY, 1986.
[53] S.K. Wang, S.-j. Lee, O.C. Jones Jr., R.T. Lahey Jr., 3-D turbulence structure and phase distribution measurements in bubbly two-phase flows, Int. J. Multiphase Flow 13 (3) (1987).
[54] S.P. Antal, R.T. Lahey, J.E. Flaherty, Analysis of phase distribution in fully developed laminar bubbly two-phase flows, Int. J. Multiphase Flow 17 (5) (1991) 635–652.
[55] Y. Sato, M. Sadatomi, K. Sekoguchi, Momentum and heat transfer in two-phase bubble flow, in: International Journal of Multiphase Flow, I. Theory, pp. 167–177. II. A Comparison Between Experiment and Theoretical Calculations, 1981, pp. 179–190.
[56] M. Lopez de Bertodano, S.-J. Lee, R.T. Lahey Jr., D.A. Drew, The prediction of two-phase turbulence and phase distribution phenomena using a Reynolds stress model, J. Fluids Eng. 112 (1990) 107–113.
[57] M. Lopez de Bertodano, R.T. Lahey Jr., O.C. Jones, Development of a k–ε model for bubbly two-phase flow, J. Fluids Eng. 116 (1994) 128–134.
[58] M. Lopezde Bertodano, R.T. Lahey Jr., O.C. Jones, Phase distribution in bubbly two-phase flow in vertical ducts, Int. J. Multiphase Flow 20 (5) (1994) 805–818.
[59] V.E. Nakoryakov, O.N. Kashinsky, V.V. Randin, L.S. Timkin, Gas–liquid bubbly flow in vertical pipes, J. Fluids Eng. 118 (1996) 377–382.
[60] N. Boisson, M.R. Malin, Numerical prediction of two-phase flow in bubble columns, Int. J. Numer. Methods Fluids 23 (1996) 1289–1310.
[61] B. Huang, Modelisation Numerique D'ecoulements Diphasiques a Bulles dans les Reacteurs Chimiques, Ph.D. Thesis, Universite Claude Bernard, Lyon, 1989.
[62] K.O. Peterson, Etude Experimentale et Numerique des Ecoulements Diphasiques dans les Reacteurs Chimiques, Ph.D. Thesis, Universite Claude Bernard, Lyon, 1992.
[63] R.T. Lahey, M. Lopez de Bertodano, O.C. Jones, Phase distribution in complex geometry ducts, Nuclear Eng. Design 141 (1993) 177.

[64] D.A. Drew, T.J. Lahey Jr., The virtual mass and lift force on a sphere in rotating and straining inviscid flow, Int. J. Multiphase Flow 13 (1) (1987) 113.
[65] PHOENICS: "http://www.cham.co.uk/phoenics/d_polis/d_applic/d_flows/laheya.htm".
[66] Y. Tsuji, Y. Morikawa, H. Shiomi, LDV measurements of an air–solid two-phase flow in a vertival pipe, J. Fluid Mech. 139 (1984) 417–434.
[67] A. Adeniji-Fashola, C.P. Chen, Modeling of confined turbulent fluid-particle flows using Eulerian and Lagrangian schemes, Int. J. Heat Mass Transfer 33 (1990) 691–701.
[68] S. Naik, I.G. Bryden, Prediction of turbulent gas–solids flow in curved ducts using the Eulerian–Lagrangian method, Int. J. Numer. Methods Fluids 31 (1999) 579–600.
[69] F.H. Harlow, A.A. Amsden, Numerical calculation of multiphase fluid flow, J. Comput. Phys. 17 (1975) 19–52.
[70] A.N. Osiptsov, Structure of the laminar boundary layer of a disperse medium on a flat plate, Fluid Dynamics 15 (1980) 512–517.
[71] S. Prabha, A.C. Jain, On the use of compatibility conditions in the solution of gas particulate boundary layer equations, Appl. Sci. Res. 36 (1980) 81–91.
[72] R.E. Sgleton, The incompressible gas solid particle flows over a semi-infinite flat plate, Z. Angew. Math. Phys. 19 (1965) 545.
[73] B.Y. Wang, I.I. Glass, Compressible laminar boundary layer flows of a dusty gas over a semi-infinite flat plate, J. Fluid Mech. 186 (1988) 223–241.
[74] S.L. Soo, Boundary layer motion of a gas–solids suspension, in: Proc. Symp. Interaction Between Fluids and Particles, Inst. Chem. Eng., 1962, pp. 50–63.
[75] A.J. Chamkha, J.J.R. Peddieson, Boundary layer flow of a particulate suspension past a flat plate, Int. J. Multiphase Flow 17 (1991) 805–808.
[76] N. Thevand, E. Daniel, J.C. Loraud, On high-resolution schemes for solving unsteady compressible two-phase dilute viscous flows, Int. J. Numer. Methods Fluids 31 (1999) 681–702.
[77] I.S. Chang, One and two-phase nozzle flows, AIAA J. 18 (1980) 1455–1461.
[78] R. Ishii, K. Kawasaki, Limiting particle streamline in the flow of a gas–particle mixture through an axially symmetric nozzle, Phys. Fluids 25 (6) (1982) 959–966.
[79] R. Ishii, Y. Umeda, K. Kawasaki, Nozzle flows of gas–particle mixtures, Phys. Fluids 30 (3) (1987) 752–760.
[80] C.J. Hwang, G.C. Chang, Numerical study of gas–particle flow in a solid rocket nozzle, AIAA J. 26 (6) (1988) 682–689.
[81] H.T. Chang, L.W. Hourng, L.E. Chien, Application of flux-vector-splitting scheme to a dilute gas–particle JPL nozzle flow, Int. J. Numer. Methods Fluids 22 (1996) 921–935.
[82] R.C. Mehta, T. Jayachandran, A fast algorithm to solve viscous two-phase flow in an axisymmetric rocket nozzle, Int. J. Numer. Methods Fluids 26 (1998) 501–517.
[83] O. Igra, I. Elperin, G. Ben-Dor, Dusty gas flow in a converging–diverging nozzle nozzle, J. Fluids Eng. 121 (1999) 908–913.
[84] L.H. Back, R.F. Cuffel, Detection of oblique shocks in a conical nozzle with a circular-arc throat, AIAA J. 4 (1966) 2219–2221.
[85] L.H. Back, P.F. Massier, R.F. Cuffel, Flow phenomena and convective heat transfer in a conical supersonic nozzle, J. Spacecraft 4 (1967) 1040–1047.
[86] R.F. Cuffel, L.H. Back, P.F. Massier, Transonic flowfield in a supersonic nozzle with small throat radius of curvature, AIAA J. 7 (1969) 1364–1366.